IOP Publishing Journal of Neural Engineering
J. Neural Eng. 13 (2016) 016005 (14pp) doi:10.1088/1741-2560/13/1/016005

Source-space ICA for MEG source imaging

Yaqub Jonmohamadi[1,2] and Richard D Jones[2,3,4]

[1] Department of Physics, University of Auckland, Auckland, New Zealand
[2] New Zealand Brain Research Institute, Christchurch, New Zealand
[3] Department of Medicine, University of Otago, Christchurch, New Zealand
[4] Department of Electrical and Computer Engineering, University of Canterbury, Christchurch, New Zealand

E-mail: y.jonmo@auckland.ac.nz

Received 4 May 2015, revised 25 October 2015
Accepted for publication 29 October 2015
Published 8 December 2015

Abstract

Objective. One of the most widely used approaches in electroencephalography/magnetoencephalography (MEG) source imaging is application of an inverse technique (such as dipole modelling or sLORETA) on the component extracted by independent component analysis (ICA) (sensor-space ICA + inverse technique). The advantage of this approach over an inverse technique alone is that it can identify and localize multiple concurrent sources. Among inverse techniques, the minimum-variance beamformers offer a high spatial resolution. However, in order to have both high spatial resolution of beamformer and be able to take on multiple concurrent sources, sensor-space ICA + beamformer is not an ideal combination. *Approach*. We propose source-space ICA for MEG as a powerful alternative approach which can provide the high spatial resolution of the beamformer and handle multiple concurrent sources. The concept of source-space ICA for MEG is to apply the beamformer first and then singular value decomposition + ICA. In this paper we have compared source-space ICA with sensor-space ICA both in simulation and real MEG. The simulations included two challenging scenarios of correlated/concurrent cluster sources. *Main Results*. Source-space ICA provided superior performance in spatial reconstruction of source maps, even though both techniques performed equally from a temporal perspective. Real MEG from two healthy subjects with visual stimuli were also used to compare performance of sensor-space ICA and source-space ICA. We have also proposed a new variant of minimum-variance beamformer called weight-normalized linearly-constrained minimum-variance with orthonormal lead-field. *Significance*. As sensor-space ICA-based source reconstruction is popular in EEG and MEG imaging, and given that source-space ICA has superior spatial performance, it is expected that source-space ICA will supersede its predecessor in many applications.

Keywords: beamformer, MEG, independent component analysis, localization, time-course reconstruction

(Some figures may appear in colour only in the online journal)

1. Introduction

Magnetoencephalography (MEG) records magnetic activities produced by electrical currents in the brain. Compared with electroencephalography (EEG), MEG provides a better spatial resolution due to magnetic fields being less affected by skull and scalp. Both MEG and EEG have millisecond temporal resolution, which is an important advantage over other popular brain functional imaging techniques such as fMRI and PET. In localization of brain sources via EEG and MEG, a fundamental problem is that the number N of scanning points (voxels) in the 3D source-space (brain) is much greater than the number M of sensors. A major focus of inverse techniques applied to MEG and EEG is how to best handle this problem. Some of the earlier inverse techniques such as dipole fitting [1–3] rely on major assumptions, such as the source of interest for a given time window is the dominant source and, if not, the number of dominant sources are known in advance.

Such assumptions may not be true, plus dipole fitting is not able to show distributed sources. Another widely used inverse technique is minimum-norm spatial filters [4–6]. Compared with dipole fitting, they can estimate distributed sources and do not rely on an assumed number of the sources for a given MEG/EEG record. Another versatile approach to source imaging in EEG and MEG is minimum-variance filters (beamformers) [7–11]. Compared with minimum-norm filters, minimum-variance beamformers utilize the covariance matrix of the sensor signals and have been shown to be superior in spatial resolution to minimum-norm filters [12–14]. However, all of the above inverse methods are based on magnitude of the sources, i.e., they are successful when the desired sources are strong in relative to the background activity or noise. Conversely, they struggle to detect multiple concurrent sources, especially weaker sources. To overcome this limitation, approaches such as independent component analysis (ICA) and principal component analysis (PCA) have been applied to separate sources during an epoch of MEG or EEG and localize each source individually via an inverse method. ICA is a blind source separation technique which aims to separate P mutually statistically independent, zero mean, sources from M linearly combined signal mixtures [15]. In EEG and MEG, ICA has been extensively used for component extraction of event related potentials (ERPs) [16–21] and for artifact removal [22–24]. Examples of ICA application in inverse problem are ICA + dipole fitting [17] and ICA + minimum-norm filter (sLORETA) [19]. These are both examples of ICA applied on the sensor-space EEG. Recently, source-space ICA for EEG source imaging [25] was proposed. In this approach, singular value decomposition (SVD) and ICA are applied to the source-space data matrix, generated via minimum-variance beamforming (beamformer + SVD + ICA). The superiority of this approach was demonstrated over beamforming alone and ICA + dipole fitting, in terms of spatial resolution and ability to detect multiple concurrent sources. However, no direct comparison between ICA + beamformer and beamformer + SVD + ICA and it is not clear to what extent the order of application of ICA and beamformer can change source imaging performance, both spatially and temporally. In the current study, we proposed and evaluated the application of source-space ICA to MEG, with some simplifications and necessary modifications to the procedure of source-space ICA of EEG. Here we have used the orthonormal lead-field rather than x, y, and z lead-field, as the rank of the lead-field matrix via spherical modelling is always 2. We have also proposed a variant of the minimum-variance beamformer with unit-noise gain and a simpler equation compared to that of the weight-normalized minimum-variance (WNMV) beamformer [9]. The simulations includes distributed and correlated sources. We have also applied source-space ICA to the real MEG for localization of brain sources time-locked to visual stimuli. In this paper, the comparison is between *beamformer + SVD + ICA* and *ICA + beamformer* (i.e., *source-space ICA* versus *sensor-space ICA*). Throughout this paper, plain italics indicate scalars, lower-case boldface italics indicate vectors, and upper-case boldface italics indicate matrices.

2. Methods

2.1. Problem formulation

As for EEG [25], the MEG signal for K time samples $\boldsymbol{B}(t) = [\boldsymbol{b}(t_1), \boldsymbol{b}(t_2), \dots, \boldsymbol{b}(t_K)]^{\mathrm{T}}$, on M sensors, at time point t can be written as

$$\boldsymbol{b}(t) = \int \boldsymbol{L}(\boldsymbol{r})\boldsymbol{q}(\boldsymbol{r})s(t, \boldsymbol{r})\mathrm{d}(\boldsymbol{r}) + \boldsymbol{\eta}(t), \tag{1}$$

where $\boldsymbol{L}(\boldsymbol{r}) = [\boldsymbol{l}_x(\boldsymbol{r}), \boldsymbol{l}_y(\boldsymbol{r}), \boldsymbol{l}_z(\boldsymbol{r})]$ is a $M \times 3$ lead-field matrix which shows the sensitivity of scalp sensors in three orthogonal directions (x, y, z) to the source signal $s(t, \boldsymbol{r})$ located at $\boldsymbol{r} = [r_x, r_y, r_z]^{\mathrm{T}}$ (mm) with a moment of $\boldsymbol{q}(\boldsymbol{r}) = [q_x(\boldsymbol{r}), q_y(\boldsymbol{r}), q_z(\boldsymbol{r})]^{\mathrm{T}}$ (A. m), and $\boldsymbol{\eta}(t)$ is the additive noise. The reconstructed time-course, $\hat{\boldsymbol{s}}(t, \boldsymbol{r}) = [\hat{s}_x(t, \boldsymbol{r}), \hat{s}_y(t, \boldsymbol{r}), \hat{s}_z(t, \boldsymbol{r})]^{\mathrm{T}}$, for a given location $\boldsymbol{r}$ to the vector spatial filter can be written as

$$\hat{\boldsymbol{s}}(t, \boldsymbol{r}) = \boldsymbol{W}^{\mathrm{T}}(\boldsymbol{r})\boldsymbol{b}(t), \tag{2}$$

where $\boldsymbol{W}(\boldsymbol{r}) = [\boldsymbol{w}_x(\boldsymbol{r}), \boldsymbol{w}_y(\boldsymbol{r}), \boldsymbol{w}_z(\boldsymbol{r})]$ is a $M \times 3$ matrix of the vector spatial filter coefficients. One way to obtain a tomographic map for all brain locations (voxels), for a given EEG/MEG segment, is to estimate the power in each voxel

$$\begin{aligned} \boldsymbol{p}_\xi(\boldsymbol{r}) &= \boldsymbol{w}_\xi^{\mathrm{T}}(\boldsymbol{r})\boldsymbol{C}\boldsymbol{w}_\xi(\boldsymbol{r}) = \left\langle \hat{s}_\xi(t, \boldsymbol{r})^2 \right\rangle, \\ &\xi \in x, y, z; \ \boldsymbol{r} \in \Omega, \end{aligned} \tag{3}$$

where $\langle ... \rangle$ is the ensemble average, Ω is the locations of the 3D scanning grid covering the whole brain (source-space), and $\boldsymbol{C}$ is the covariance matrix

$$\boldsymbol{C} = \left\langle \boldsymbol{b}(t)\boldsymbol{b}^{\mathrm{T}}(t) \right\rangle. \tag{4}$$

The lead-field matrix computed using the spherical head model (which is very popular for MEG) for every voxel has a rank of 2 [2, 26]. Therefore, using SVD we can reduce the size of the lead-field to $M\times$ 2. The SVD of $\boldsymbol{L}(\boldsymbol{r})$ can be written as

$$\boldsymbol{L} = \boldsymbol{U}\boldsymbol{\Sigma}\boldsymbol{V}^{\mathrm{T}}, \tag{5}$$

where $\boldsymbol{U}$ and $\boldsymbol{V}^{\mathrm{T}}$ are $M \times M$ and 3×3 unitary matrices respectively and $\boldsymbol{\Sigma}$ is an $M \times 3$ diagonal matrix with the diagonal elements being the singular values on descending order. As the rank of the lead-field is 2, the third diagonal element of the $\boldsymbol{\Sigma}$ is 0. To reduce the size of the lead-field, the first two column vectors of $\boldsymbol{U}$, corresponding to the two principal orientations (POs), can be used as the new lead-field (orthonormal lead-field)

$$\boldsymbol{L}'(\boldsymbol{r}) = \left[\boldsymbol{u}_1(\boldsymbol{r}), \boldsymbol{u}_2(\boldsymbol{r})\right] = \left[\boldsymbol{l}'_{\mathrm{PO1}}(\boldsymbol{r}), \boldsymbol{l}'_{\mathrm{PO2}}(\boldsymbol{r})\right], \boldsymbol{L}'(\boldsymbol{r}) \in \Re^{(M\times 2)}. \tag{6}$$

2.2. Beamformer

There are several variants of minimum-variance beamformers [12], in which the weight matrix is derived based upon different constraints. In the case of source-space ICA it is necessary for the beamformer to have a uniform white-noise spatial map (in other words, unit-noise gain constraint). This means that the beamformer must satisfy the constraint

$$\boldsymbol{W}^{\mathrm{T}}(\boldsymbol{r})\boldsymbol{W}(\boldsymbol{r}) = \boldsymbol{I}, \tag{7}$$

where $\boldsymbol{I}$ is the identity matrix. Using the normalized lead-field for the well known linearly-constrained minimum-variance (LCMV) beamformer does not result in a normalized white-noise spatial map [14] and the neural activity index (NAI) is needed to compensate this [7, 10]. However, the WNMV beamformer proposed by [9] (also known as Borgiotti–Kaplan) satisfies the constraint of a normalized white-noise spatial map. Conversely, compared with LCMV, the weight matrix equation for the WNMV beamformer is more complicated and uses the second order of the inverse covariance matrix which, from our experience, can result in numerical issues (e.g., imaginary elements may appear for the second order of the inverse covariance matrix). Therefore, it is preferable to avoid the WNMV beamformer when alternatives are available. Here we derive a new version of the minimum-variance beamformer, which is as simple as LCMV but still has a normalized white-noise spatial map. This beamformer is based on normalization of the weight vectors of LCMV and therefore we abbreviate it as WNLCMV. Similar to [7], the weight matrix for LCMV beamformer is

$$\boldsymbol{W}_{\mathrm{LCMV}}(\boldsymbol{r}) = \frac{\boldsymbol{C}^{-1}\boldsymbol{L}(\boldsymbol{r})}{\boldsymbol{L}^{\mathrm{T}}(\boldsymbol{r})\boldsymbol{C}^{-1}(\boldsymbol{r})\boldsymbol{L}(\boldsymbol{r})}, \tag{8}$$

and the WNLCMV beamformer is obtained by normalizing the LCMV weight vectors

$$\boldsymbol{W}_{\mathrm{WNLCMV}}(\boldsymbol{r}) = \left[\frac{\boldsymbol{w}_{\mathrm{LCMV}-x}}{||\boldsymbol{w}_{\mathrm{LCMV}-x}||}, \frac{\boldsymbol{w}_{\mathrm{LCMV}-y}}{||\boldsymbol{w}_{\mathrm{LCMV}-y}||}, \frac{\boldsymbol{w}_{\mathrm{LCMV}-z}}{||\boldsymbol{w}_{\mathrm{LCMV}-z}||}\right], \tag{9}$$

which satisfies the constraint of equation (7) and has a uniform white-noise spatial map. Using the spherical head model and orthonormal lead-field of equation (6) for LCMV, the WNLCMV can be written as

$$\boldsymbol{W}_{\mathrm{WNLCMV}}(\boldsymbol{r}) = \left[\frac{\boldsymbol{w}_{\mathrm{LCMV-PO1}}}{||\boldsymbol{w}_{\mathrm{LCMV-PO1}}||}, \frac{\boldsymbol{w}_{\mathrm{LCMV-PO2}}}{||\boldsymbol{w}_{\mathrm{LCMV-PO2}}||}\right], \tag{10}$$

where PO1 and PO2 refers to two POs. Using this WNLCMV beamformer for source imaging, one does not need to use the NAI and can estimate the power at each voxel for an epoch of data by

$$\langle|\hat{s}(t, \boldsymbol{r})|\rangle = \sqrt{\left\langle tr\left\{\boldsymbol{W}^{\mathrm{T}}(\boldsymbol{r})\boldsymbol{b}(t)\boldsymbol{b}^{\mathrm{T}}(t)\boldsymbol{W}(\boldsymbol{r})\right\}\right\rangle}\ , \tag{11}$$

where $\boldsymbol{W} = \boldsymbol{W}_{\mathrm{WNLCMV}}$. The magnitude time-series of each voxel via WNLCMV beamformer is obtained via

$$\begin{aligned}|\hat{s}(t, \boldsymbol{r})| &= \sqrt{tr\left\{\boldsymbol{W}^{\mathrm{T}}(\boldsymbol{r})\boldsymbol{b}(t)\boldsymbol{b}^{\mathrm{T}}(t)\boldsymbol{W}(\boldsymbol{r})\right\}}\\ &= \sqrt{\hat{s}_{\mathrm{PO1}}^{2}(t, \boldsymbol{r}) + \hat{s}_{\mathrm{PO2}}^{2}(t, \boldsymbol{r})}\ ,\end{aligned} \tag{12}$$

which is also simpler than the equation for the NAI as used by [7] and [10].

2.3. Source-space ICA (beamforming + SVD + ICA)

Compared with the EEG version with its *x, y,* and *z* time-courses for each voxel, source-space ICA for MEG has only two time-courses, corresponding to the two POs (PO1 and PO2) obtained following the SVD of the lead-field. Therefore, the reconstructed source-space data matrix $\hat{\boldsymbol{S}} \in \Re^{(2N\times K)}$ for all N voxels and K time samples via the WNLCMV is

$$\hat{\boldsymbol{S}} = \begin{pmatrix} \hat{s}_{\mathrm{PO1}}(t_1, \boldsymbol{r}_1) & \hat{s}_{\mathrm{PO1}}(t_2, \boldsymbol{r}_1) & \cdots & \hat{s}_{\mathrm{PO1}}(t_K, \boldsymbol{r}_1)\\ \hat{s}_{\mathrm{PO2}}(t_1, \boldsymbol{r}_1) & \hat{s}_{\mathrm{PO2}}(t_2, \boldsymbol{r}_1) & \cdots & \hat{s}_{\mathrm{PO2}}(t_K, \boldsymbol{r}_1)\\ \hat{s}_{\mathrm{PO1}}(t_1, \boldsymbol{r}_2) & \hat{s}_{\mathrm{PO1}}(t_2, \boldsymbol{r}_2) & \cdots & \hat{s}_{\mathrm{PO1}}(t_K, \boldsymbol{r}_2)\\ \hat{s}_{\mathrm{PO2}}(t_1, \boldsymbol{r}_2) & \hat{s}_{\mathrm{PO2}}(t_2, \boldsymbol{r}_2) & \cdots & \hat{s}_{\mathrm{PO2}}(t_K, \boldsymbol{r}_2)\\ \vdots & \vdots & \ddots & \vdots\\ \hat{s}_{\mathrm{PO2}}(t_1, \boldsymbol{r}_N) & \hat{s}_{\mathrm{PO2}}(t_2, \boldsymbol{r}_N) & \cdots & \hat{s}_{\mathrm{PO2}}(t_K, \boldsymbol{r}_N) \end{pmatrix}. \tag{13}$$

We then apply SVD to the data matrix to first reduce the size of the data matrix and then separate the spatial and temporal subspaces,

$$\hat{\boldsymbol{S}} = \boldsymbol{U}\boldsymbol{\Sigma}\boldsymbol{V}^{\mathrm{T}}, \tag{14}$$

where $\boldsymbol{U}$ and $\boldsymbol{V}^{\mathrm{T}}$ are $2N \times 2N$ and $K \times K$ unitary matrices respectively and $\boldsymbol{\Sigma}$ is a $2N \times K$ diagonal matrix with its diagonal elements being the singular values in descending order. For dimensional reduction, $\hat{\boldsymbol{S}}$ is decomposed as

$$\begin{aligned}\hat{\boldsymbol{S}} &= [\boldsymbol{U}_{\mathrm{D}}\ \boldsymbol{U}_{\mathrm{UD}}]\begin{pmatrix}\boldsymbol{\Sigma}_{\mathrm{D}} & 0\\ 0 & \boldsymbol{\Sigma}_{\mathrm{UD}}\end{pmatrix}\left[\boldsymbol{V}_{\mathrm{D}}^{\mathrm{T}}\ \boldsymbol{V}_{\mathrm{UD}}^{\mathrm{T}}\right]\\ &= \boldsymbol{U}_{\mathrm{D}}\boldsymbol{\Sigma}_{\mathrm{D}}\boldsymbol{V}_{\mathrm{D}}^{\mathrm{T}} + \boldsymbol{U}_{\mathrm{UD}}\boldsymbol{\Sigma}_{\mathrm{UD}}\boldsymbol{V}_{\mathrm{UD}}^{\mathrm{T}} = \hat{\boldsymbol{S}}_{\mathrm{D}} + \hat{\boldsymbol{S}}_{\mathrm{UD}},\end{aligned} \tag{15}$$

where $\hat{\boldsymbol{S}}_{\mathrm{D}}$ is the desired subspace of the source-space data matrix and $\hat{\boldsymbol{S}}_{\mathrm{UD}}$ is the undesired subspace containing noise only. $\boldsymbol{\Sigma}_{\mathrm{D}}$ contains the first M' singular values and $M' \leqslant M$. Therefore, to define M', the rank test for the data matrix was used, $M' = \mathrm{rank}(\hat{\boldsymbol{S}})$. ICA is applied on the temporal subspace, $\boldsymbol{Y} = \boldsymbol{\Sigma}_{\mathrm{D}}\boldsymbol{V}_{\mathrm{D}}^{\mathrm{T}}$, $\boldsymbol{Y} \in \Re^{(M'\times K)}$, and it estimates the independent components and the unmixing matrix

$$\bar{\boldsymbol{S}} = \boldsymbol{H}\boldsymbol{Y}, \tag{16}$$

where $\boldsymbol{H} \in \Re^{(M'\times M')}$ is the unmixing matrix, $\bar{\boldsymbol{S}}$ is the matrix of independent components and the *i*th row of $\bar{\boldsymbol{S}} = [\bar{s}_1, \bar{s}_2, ..., \bar{s}_{M'}]^{\mathrm{T}}$ is the time-series of the *i*th independent component. The tomographic maps of M' identified components in $\bar{\boldsymbol{S}}$ can be obtained by multiplication of the spatial subspace $\boldsymbol{U}_{\mathrm{D}} \in \Re^{(2N\times M')}$ by the mixing matrix $\boldsymbol{H}^{-1}$

$$\boldsymbol{G} = \boldsymbol{U}_{\mathrm{D}}\boldsymbol{H}^{-1}, \tag{17}$$

where the *i*th column of $\boldsymbol{G} = [\boldsymbol{g}_1, \boldsymbol{g}_2, ..., \boldsymbol{g}_{M'}] \in \Re^{(2N\times M')}$ shows the 3D map for the *i*th row of $\bar{\boldsymbol{S}}$. However, for each location $\boldsymbol{r}$, the column vector $\boldsymbol{g}_i$ has 2 coefficients (PO1 and PO2) corresponding to the vector beamformer

$$\begin{aligned}\boldsymbol{g}_i &= \left[g_{i-\mathrm{PO1}}(\boldsymbol{r}_1), g_{i-\mathrm{PO2}}(\boldsymbol{r}_1), g_{i-\mathrm{PO1}}(\boldsymbol{r}_2), g_{i-\mathrm{PO2}}(\boldsymbol{r}_2),\right.\\ &\quad \left.\times \ldots, g_{i-\mathrm{PO2}}(\boldsymbol{r}_N)\right]^{\mathrm{T}},\\ i &= 1, \ldots, M'.\end{aligned} \tag{18}$$

To obtain a single value for each location, vector addition is applied onto orthogonal values

$$|g_i(\boldsymbol{r}_n)| = \sqrt{g_{i-\mathrm{PO1}}^2(\boldsymbol{r}_n) + g_{i-\mathrm{PO2}}^2(\boldsymbol{r}_n)}\ , \quad n = 1, 2, \dots, N, \tag{19}$$

and

$$\hat{\boldsymbol{g}}_i = \left[\left|g_i(\boldsymbol{r}_1)\right|, \left|g_i(\boldsymbol{r}_2)\right|, \dots, \left|g_i(\boldsymbol{r}_N)\right|\right]^{\mathrm{T}}, \ i = 1, 2, \dots, M'. \tag{20}$$

The tomographic map of the ith component in $\bar{\boldsymbol{S}}$, i.e., $\bar{\boldsymbol{s}}_i$, is obtained by projecting the vector $\hat{\boldsymbol{g}}_i$ to the 3D scanning grid. The location of the voxel in the source-space with maximum intensity for the ith component is

$$\boldsymbol{r}_{\max} = \mathrm{argmax}_{\boldsymbol{r}_n}\left(\left|g_i(\boldsymbol{r}_n)\right|\right), \ n = 1, 2, \dots, N. \tag{21}$$

2.4. Sensor-space ICA (ICA + beamforming)

In this approach, similar to that of [17] and [19], ICA is applied to the sensor data $\boldsymbol{B}(t)$ and then the inverse technique is applied to the columns of the mixing matrix corresponding to the time-courses of interest

$$\boldsymbol{S}' = \boldsymbol{H}\boldsymbol{B}, \tag{22}$$

where $\boldsymbol{H} \in \Re^{(M \times M)}$ is the unmixing matrix, $\boldsymbol{S}' \in \Re^{(M \times K)}$ is the matrix of independent components and the ith row of $\boldsymbol{S}' = [\boldsymbol{s}_1', \boldsymbol{s}_2', \dots, \boldsymbol{s}_M']^{\mathrm{T}}$ is the time-series of the ith independent component. Assuming $\boldsymbol{Z}$ is the tomographic map of the ith identified component in $\boldsymbol{S}'$, the intensity at $\boldsymbol{r}$ for the tomographic map of ith identified component in $\boldsymbol{S}'$ can be obtained by multiplication of the ith column of the $\boldsymbol{H}^{-1}$ by the beamformer weight matrix $\boldsymbol{W}$

$$z(\boldsymbol{r}_n) = \sqrt{\begin{array}{l}\left(\boldsymbol{w}_{\mathrm{WNLCMV-PO1}}^{\mathrm{T}}(\boldsymbol{r}_n)\boldsymbol{h}_i^{-1}\right)^2 \\ +\left(\boldsymbol{w}_{\mathrm{WNLCMV-PO2}}^{\mathrm{T}}(\boldsymbol{r}_n)\boldsymbol{h}_i^{-1}\right)^2\end{array}}, \quad n = 1, 2, \dots, N. \tag{23}$$

To calculate the beamformer weight matrix, when the input signal is only the vector of the mixing matrix (single point input data), instead of inverse covariance matrix ($\boldsymbol{C}^{-1}$), the regularized inverse covariance matrix ($(\boldsymbol{C} + \gamma\boldsymbol{I})^{-1}$) must be used, as the rank of the mixing vector is 1. We used $\gamma = 0.001\lambda_1$ as the regularization factor, and λ_1 is the largest eigenvalue of $\boldsymbol{C}$ [9]. The regularized inverse increases the SNR of the beamformer [8, 27, 28] but leads to higher interference from other sources close to the source of interest signal and reduces the spatial resolution.

3. Simulated and real MEG sources

The background MEG for simulated sources was real MEG from three healthy subjects, recorded during the resting state in another study [29]. The 275-channel CTF MEG system (MEG International Series Ltd, Coquitlam, BC, Canada) was used at a sampling frequency of 6000 Hz and band-pass filtered at 1–45 Hz. The single-layer spherical head model, implemented in FieldTrip toolbox [30], was used for the computation of the lead-field. The conductivity ratio of skull to soft tissue was 0.0125. Infomax [31] was applied for ICA. The 3D scanning grid divides the brain into 4040 voxels, each of $8 \times 8 \times 8$ mm. Performance was estimated via the correlation between the maps provided by source-space ICA and sensor-space ICA and ground truth. As source-space ICA involves application of SVD and ICA post-beamforming, we also refer to it as beamforming + SVD + ICA, and we refer to sensor-space ICA as ICA + beamforming. The aim is evaluate how the change in the order of application of these two techniques (ICA and beamforming) can alter the outcome of source imaging.

3.1. Simulated MEG sources

3.1.1. Concurrent sources. Here we undertook two simulations: (1) two sinusoidal cluster sources concurrently active for 3 s at 6 Hz and at 10 Hz, (2) two sinusoidal cluster sources concurrently active for 3 s with both at 10 Hz. The second simulation is the worst case scenario for the beamformers as the two sources are 100% correlated. Furthermore, we repeated the two simulations with different SNRs and orientations of the sources superimposed on background MEG from three healthy subjects. There were seven samples of the simulated cluster sources with SNR from 0.13 to 3.00 and eight orientations for each of the cluster sources corresponding to 180° change in orientation. Therefore, each of these two simulations was repeated $7 \times 8 \times 3 = 168$ times. Each cluster comprised 45 voxels ($5 \times 3 \times 3$). The center of the two cluster sources are at [−22, −14, 32] mm and [20, −58, 32] mm (MNI coordinates).

The motivation for this simulation is due to the differences observed in the source imaging via source-space ICA compared with sensor-space ICA for the real MEG of subjects with visual stimulation. As we will show in the section 4 for real MEG, even though ICA identified similar time-courses for both techniques, localizations via these two techniques for some of the components were significantly different. In order to identify which approach estimates the correct source localization, we conducted this simulation with concurrently active cluster sources.

3.1.2. Quantitative performance measurement. In this simulation, a single sinusoidal (10 Hz) source was evaluated under poor SNRs and different depths and orientations. The SNR of the simulated source was set 0.01–0.35 (ten SNR samples). The orientation of the source was also varying from 0° to 180° around z axis (seven orientation samples). And the depth of the source was from ∼10 mm to ∼110 mm (eight depth samples) corresponding to [0, 0, 2] mm to [0, 0, 98] mm locations. The diameter of the spherical head model was 110 mm. This simulation was performed on the background from three subjects. Therefor, this simulation is repeated 1680 times.

3.2. Real MEG sources

To demonstrate and compare the application of source-space ICA for localization and time-course reconstruction of real MEG sources, real MEG data (CTF 275 channel) were downloaded from the SPM website (www.fil.ion.ucl.ac.uk/spm/data/mmfaces). The MEG data from two healthy subjects comprise 168 visual event-related fields (ERF) from 84 faces and 84 scrambled faces. Only the 84 ERFs for the faces were used in the current study. The covariance matrix for the beamformer was calculated over the 84 concatenated ERFs (84~×~800 ms), in line with other literature [24, 32–34]. To identify the components of sensor- and source-space ICA which have activity associated with the visual ERFs, the components were averaged over 84 trials to obtain single-trial components and then rectified. A Pearson correlation test was then applied between the averaged rectified components and a reference signal, to identify components with higher magnitudes during the 0–300 ms post-stimulus. The reference signal was a rectangular pulse of magnitude 1 from 0 to 300 ms and zero otherwise over the interval −200 to 600 ms; that is, 0 to 300 ms is tha window in which the sources of the visual ERFs were expected to be substantially active). Components correlated with the reference signals were interpreted as sources due to the visual stimulus.

4. Results

4.1. Simulated sources

For evaluation of the source maps obtained via sensor-space ICA and source-space ICA for the simulated cluster sources, Pearson correlation coefficients between the estimated maps via the techniques and the ground truth were calculated and provided as a measure of performance. Using this measurement one should consider that both localization error and the blurry images can reduce the correlation coefficient.

4.1.1. Two concurrent cluster sources with frequencies of 6 and 10 Hz. For each of the background activities of the three subjects, this simulation was repeated 56 times, comprising 7 SNRs and 8 orientations. For source identification, in the case of sensor-space ICA and source-space ICA, after each iteration a Pearson correlation test was calculated between the rectified time-course of the components and the rectified reference signals (the actual 6 and 10 Hz source signals) and the two time-courses which had the highest correlation coefficients were considered to be the sources of interest and their spatial maps were then estimated. The 56 maps were then averaged and Pearson correlations calculated between the ground truth and the averaged maps. Therefore, three correlation coefficients were obtained corresponding to the three backgrounds for each of the two techniques (table 1). Figure 1 shows the source imaging result for the simulated cluster sources on the background activity of subject 2. For this simulation, source-space ICA had a higher performance due to its higher spatial resolution, rather than accuracy of localization, compared with the more blurry images from sensor-space ICA. However, in the case of time-course reconstruction, both techniques performed similarly and were unable to separate the 6 and 10 Hz time-courses and, instead, separated the subtraction and summation time-courses (figure 2). This simulation, however, is a challenging scenario as both time-courses were 100% concurrent, were spatially close to each other, and had reasonably close frequencies, which made it difficult for ICA to separate. As two time-courses were identified by ICA, two spatial maps are reported for this simulation, and the spatial map of each time-course shows the map of two clusters (figure 1). For source-space ICA, the spatial map of each time-course showed two separate clusters (e.g., figure 1(b)), whereas for sensor-space ICA only one time-course had two separate clusters, with the other time-course resulting in merged clusters (e.g., figure 1(c)).

Table 1. Summary of results for two concurrent 6 and 10 Hz sinusoidal cluster sources.

Background from	Source-space ICA	Sensor-space ICA
Subject 1	$r_1 = 0.52$	$r_1 = 0.31$
	$r_2 = 0.48$	$r_2 = 0.20$
Subject 2	$r_1 = 0.53$	$r_1 = 0.30$
	$r_2 = 0.48$	$r_2 = 0.22$
Subject 3	$r_1 = 0.52$	$r_1 = 0.27$
	$r_2 = 0.46$	$r_2 = 0.25$
Average	$r_1 = 0.52$	$r_1 = 0.29$
	$r_2 = 0.47$	$r_2 = 0.22$

Note: r_1 and r_2 are the averaged correlation coefficients obtained from Pearson correlation test between ground truth and spatial maps of components 1 and 2, respectively.

4.1.2. Two concurrent cluster sources with frequency of 10 Hz. This simulation was the same as the previous simulation except for the two cluster sources being 100% correlated (both active at the same time and of identical 10 Hz sinusoidal waveform). As with the previous simulation, following each source identification a Pearson correlation test was performed between the rectified time-series of the components and rectified reference signal (the actual 10 Hz source signal). The time-course with the highest correlation coefficient was considered as the source of interest and its spatial maps then estimated. This means that for the ICA approaches there will be one spatial map as there are two sources with the same frequency and ICA was not able to separate the time-courses of the two sources. Table 2 shows the correlation coefficients obtained via the two techniques for this simulation. Figure 3 shows the source imaging results for the simulated cluster sources on the background activity of subject 2. For this simulation, source-space ICA achieved a higher performance compared to sensor-space ICA. Source-space ICA was able to localize the posterior source but the

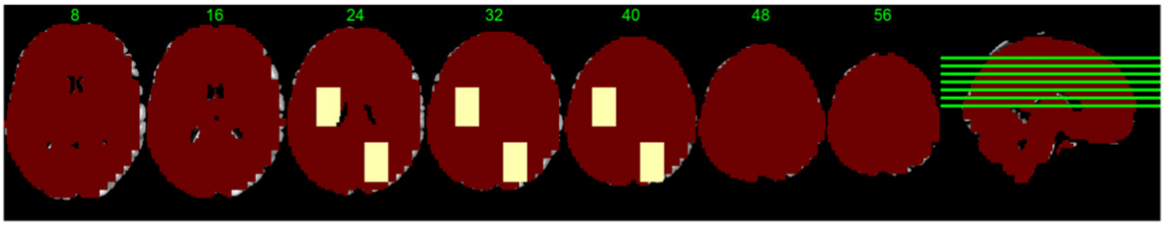

(a) Ground truth (two cluster sources)

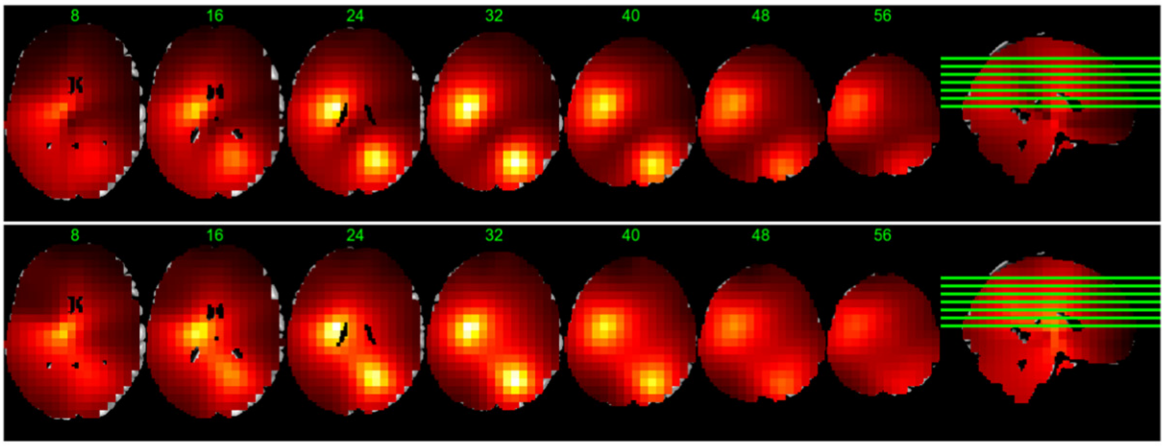

(b) Components 1 and 2 from source-space ICA

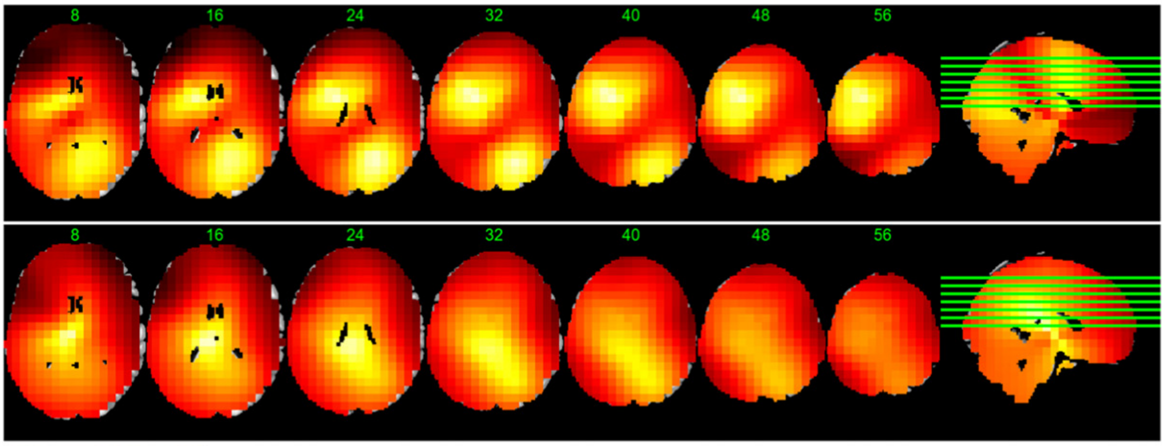

(c) Components 1 and 2 from sensor-space ICA

Figure 1. Source imaging via source-space ICA and sensor-space ICA for two concurrent cluster sources of 6 Hz and 10 Hz. The center of the two cluster sources are at [−22, −14, 32] mm and [20, −58, 32] mm (MNI coordinates). The background MEG was from subject 2. The Pearson correlation coefficients between the ground truth and the maps are provided in table 1.

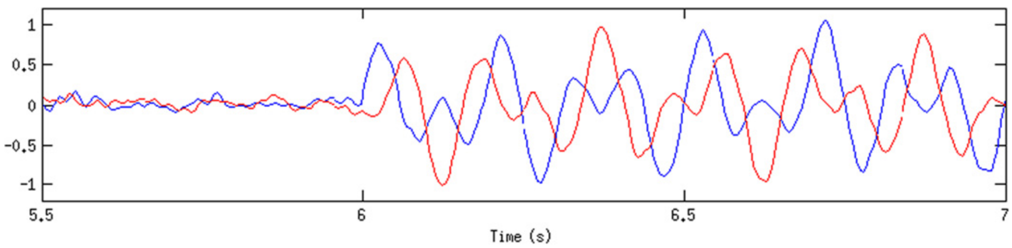

Figure 2. A example of sensor-space ICA on separation of the 6 and 10 Hz cluster sources. Both approaches were unable to separate the two time-courses with each reconstructed time-course being a mixture (subtraction and summation of the two original time-courses). Source-space ICA also showed the same behaviour.

Table 2. Summary of results for two concurrent 10 Hz sinusoidal cluster sources.

Background from	Source-space ICA	Sensor-space ICA
Subject 1	$r = 0.29$	$r = 0.24$
Subject 2	$r = 0.28$	$r = 0.20$
Subject 3	$r = 0.29$	$r = 0.25$
Average	$r = 0.29$	$r = 0.23$

frontal cluster was incorrectly estimated to be between the two actual clusters. Sensor-space ICA incorrectly estimated them to be a single source between the two clusters.

4.1.3. Quantitative performance measurement. Result of this simulation is obtained after 1680 times iteration of a simulated source (10 Hz) under varying SNR (ten samples from 0.01 to 0.35), eight depths (distance from 2 to 98 mm from the center of the sphere), and seven samples of the orientations (from 0° to 180° around z axis). The mentioned simulation was performed on background MEG of three subjects. Figure 4 shows the performance of the sensor-space ICA and source-space ICA in terms of localization error in mm. While overall localization error of source-space ICA (5 mm as shown in figures 4(b) and (c)) is lower than sensor-space ICA (Ĩ 3 mm as shown in figures 4(b) and (c)), the source-space ICA is also less affected by changes in orientation and depth of the simulated source. Based on figure 4(a) the source-space ICA achieves localization error of less than 2 mm when the SNR of the source becomes greater than 0.10, whereas the localization error for sensor-space ICA did not reach less than 10 mm.

4.2. Real MEG with ERFs

For real MEG, two important steps—semi-averaging and PCA—were considered before ICA. Semi-averaging was to average each event three times, without reducing the number of the events, i.e., after semi-averaging there were still 84 events to be given to the ICA approaches. So each of the 84 events was the average of itself and another two events from the other events. This improves the SNR of the sources and helps ICA to identify them as independent sources. Keeping the number of events at 84 rather than reducing it to fewer highly-averaged events is also another way to improve the ICA separation power. Another important factor in ICA of MEG is the rank of the MEG signal matrix. The rank test showed that the MEG data matrix was full rank even after semi-averaging of the events. However, the rank test may not be accurate using the software. Therefore, we applied PCA before ICA to reduce the number of components. We chose 70 components for PCA. By this approach, both sensor-space ICA and source-space ICA were able to separate five time-courses time-locked to the 0–300 ms post-stimuli, whereas applying the raw MEG to the ICA resulted only in two time-locked components. The average ERFs for the 274 channels for two subjects are shown in figures 6(a) and (b). The left column in figure 6 is for subject 1 and the right column for subject 2. The time-courses of the five components identified by sensor-space ICA and source-space ICA are shown in figures 6(c) and (d). These time-courses are fully averaged but the semi-averaged events were given to ICA. To identify the components time-locked to the ERFs, the Pearson correlation test was performed between the averaged rectified components and the reference signal being high over 0–300 ms and 0 otherwise (figure 5). These five components (IC_1, IC_2, IC_3, IC_4, IC_5) were consistent between the two subjects. The corresponding topographies via sensor-space ICA for each of these components are shown in figures 7 and 8. Both sensor-space ICA and source-space ICA separated near identical time-courses for the same subject (figures 6(b) and (c)). At the same time, the time-courses between two subjects are also very similar, in particular components 1–3, in terms of latency and shape. The peaks of these components were at latencies of 80 ms, 115 ms, 150 ms, 175 ms, and 215 ms for components 1–5 respectively. The topographic maps of the components obtained via sensor-space ICA are shown in figures 6(e)–(n). The topographic maps of components 1–4, between two subjects, are also very similar. Note that there were a few more components time-locked to the ERFs with peaks later than 300 ms, but here we only considered components with peaks at 0–300 ms post-stimuli. The time-courses shown in figures 6(b) and (c) are normalized and adjusted to have their peaks at 1. Figure 7 shows the tomographic maps obtained via source-space ICA for the components shown in figure 6. The tomographic maps of components 1–3 are near identical as expected, as their time-courses and topographic maps are similar. Component 1 is bilateral in the occipital cortex, but is more dominant on the right side (figures 7(a) and (b)). Component 2 has also a bilateral structure and more dominant on the right side on the right side of the occipital cortex (figures 7(c) and (d)). Other regions associated with component 2 are the fusiform gyrus and the temporal gyrus. Component 3 has a scattered structure in the middle occipital cortex and bilaterally fusiform gyrus (stronger on the right side) and close to brainstem (left side) (figures 7(e) and (f)). This component has a peak at 150 ms is the well known M170 (N170 for EEG) with a latency of 150–200 ms post stimuli. The pattern of the source activity for component 4 is different between two subjects (figures 7(g) and (h)): both have activation on the prefrontal cortex (on the right side), but for subject 1 there is also a strong activation in the middle occipital cortex which is not evident for subject 2. Also, for subject 2 there is activity on the left side which is not seen for subject 1. The source structure associated with component 5 is located on the right side of the prefrontal cortex (figures 7(i) and (j)). Figure 8 shows the tomographic maps obtained via sensor-space ICA for the components shown in figure 6. The tomographic maps of components 2 and 3 are similar (figures 8(c) and (d)), with the other components having little similarity between two subjects. Moreover, the tomographic maps of the component obtained via sensor-space ICA is quite different from maps obtained via source-space ICA. Sensor-space ICA provided blurry maps with activation mostly in the central brain regions which is not expected with ERFs. Such blurry and central

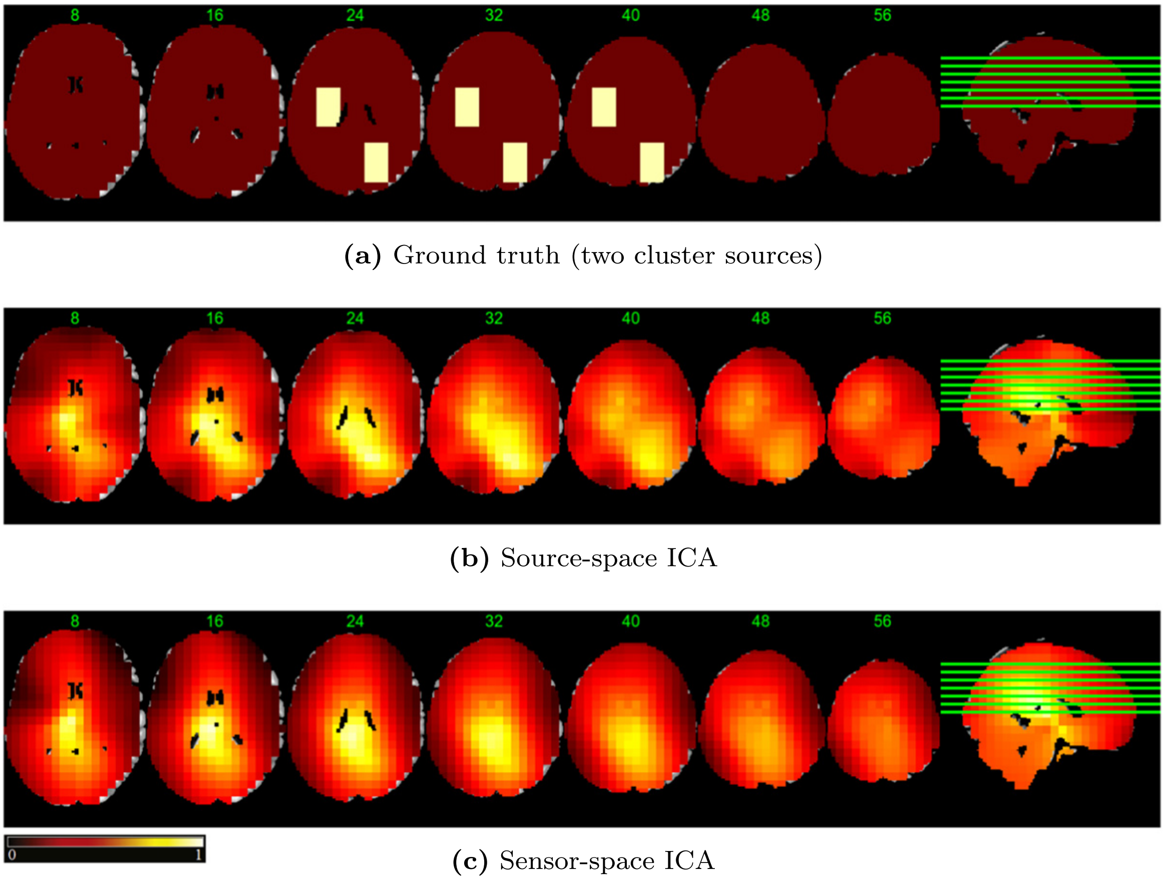

(a) Ground truth (two cluster sources)

(b) Source-space ICA

(c) Sensor-space ICA

Figure 3. Source imaging via source-space ICA and sensor-space ICA for two 100% correlated cluster sources of 10 Hz. The center of the two cluster sources are at [−22, −14, 32] mm and [20, −58, 32] mm (MNI coordinates). The background MEG was from subject 2. The Pearson correlation coefficients between the ground truth and the maps are provided in table 2.

activation patterns are similar to the simulations on the correlated cluster sources in which the sensor-space ICA was unable to separate the two cluster sources and instead merged them (figures 1(c) and 3(c)). Only component 1 of subject 1 shows a bilateral activation pattern in the occipical lobe and fusiform gyrus, where one would expect to see the sources associated with face ERFs.

5. Discussion

A common challenge for source imaging techniques, such as spatial filtering and dipole fitting, is concurrent sources. In such cases, the dominant source is most likely to appear in the map of source activity for a given EEG/MEG segment. ICA can be used to separate the concurrent sources and then inverse techniques, such as dipole fitting or minimum-norm filters, can be applied to separate sources, as shown in ICA + dipole fitting [17] and ICA + sLORETA [19]. For the case of distributed sources, dipole fitting is not appropriate. Also, minimum-norm techniques produce blurry source maps. Minimum-variance beamformers have been shown to provide higher spatial resolution than their minimum-norm counterparts. Therefore, it may appear that ICA + beamforming (sensor-space ICA) can solve the problem for both distributed sources and have a high spatial resolution. But using beamformer for components separated by ICA means that the rank of the covariance matrix (which is necessary for the beamformer) is 1 and this results in low spatial resolution for the beamformer, similar to the minimum-norm filters. Source-space ICA is an approach which captures the high spatial resolution of the beamformer and, at the same time, is able to separate and localize multiple concurrent sources. Source-space ICA: (1) applies the minimum-variance beamformer on the MEG epoch to reconstruct the time-courses on the scanning grid, (2) applies SVD for dimensional reduction and separation of the spatial and temporal subspaces of the source-space data matrix, (3) applies ICA on the temporal subspace to separate the independent time-courses, and (4) uses the mixing matrix of the ICA for the spatial subspace to provide source localization maps of the independent components. The advantage of this approach over the ICA + -beamformer (sensor-space ICA) is that the spatial resolution/accuracy of source-space ICA is superior due to the beamformer being applied on the full-rank (or near full-rank) sensor signal. Our approach used the orthonormal lead-field and a new variant of the minimum-variance beamformer. The orthonormal lead-field was obtained after SVD of the original x, y, z lead-field, and then data reduction. The rank of the lead-field calculated via the spherical model for MEG is always 2, therefore, using the orthonormal lead-field reduces the amount of the output of the vector beamformer from 3 to

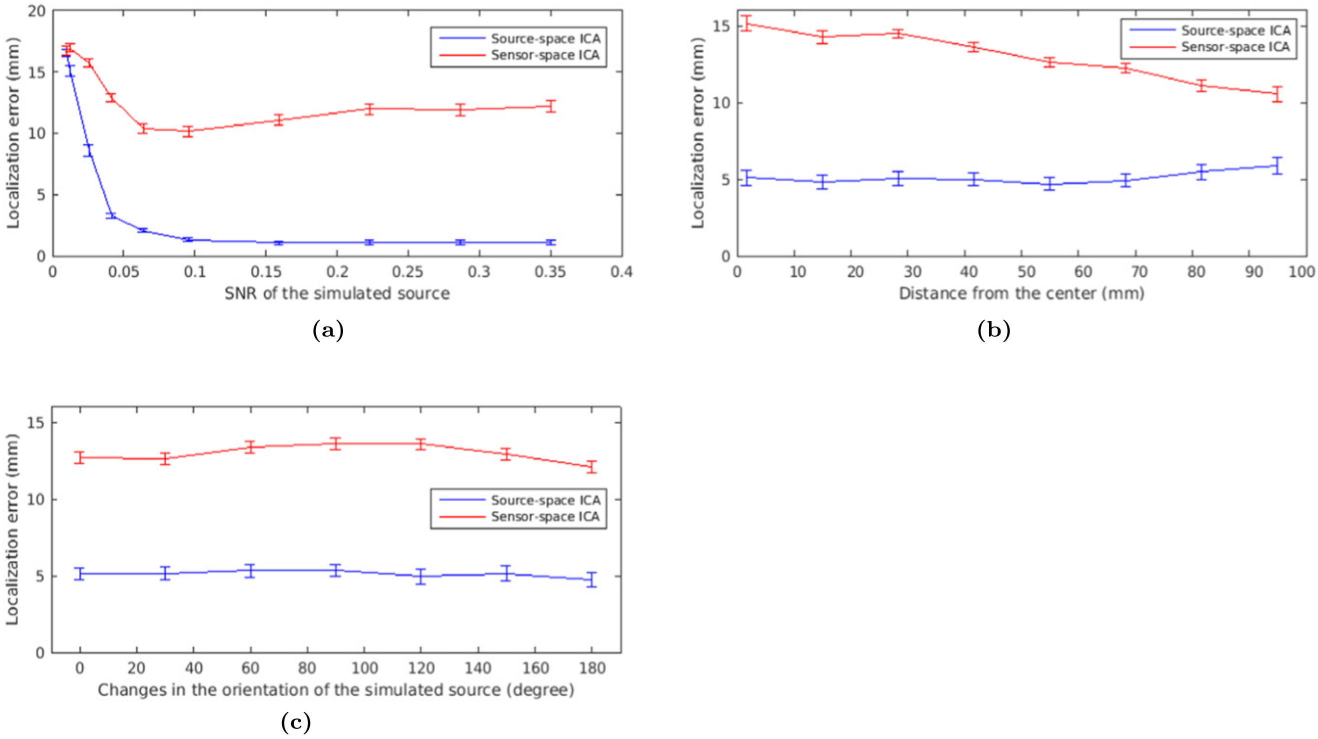

Figure 4. Performance of the source-space ICA and sensor-space ICA in terms of localization error with respect to the changes in magnitude (figure (a)), depth (figure (b)), and orientation (figure (c)) of the simulated source. The vertical bars are mean 95% confidence interval.

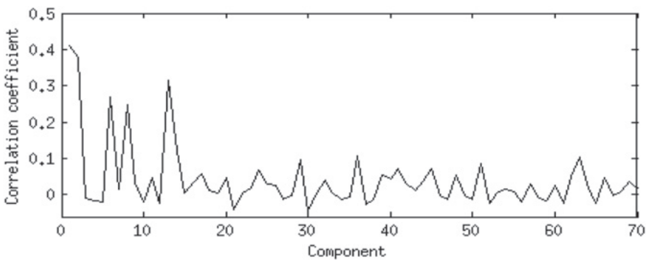

Figure 5. A typical correlation coefficient plot for the independent components separated by source-space ICA or sensor-space ICA. Several components (1, 2, 6, 8, and 13) can be seen to have correlation coefficients several times higher than other components.

2. Compared with the WNMV beamformer [9], our WNLCMV beamformer has a simpler equation and does not use the inverse covariance matrix of order 2. Similar to WNMV beamformer, the WNLCMV has a uniform white noise spatial map. This was achieved by normalization of the LCMV weight vectors. Our simulations have demonstrated the advantage of source-space ICA over sensor-space ICA. Simulations of single source reconstruction under poor SNRs and varying depth and orientation proved that the source-space ICA has a overall less localization error compared with sensor-space counterpart (i.e., 5 mm versus 13 mm). On simulation of concurrent sources we presented two scenarios which are closer to real brain sources (rather than a single point source): (1) two concurrent cluster sources, and (2) two concurrent and correlated sources. These simulations were performed with different orientations and magnitudes on the MEG background activities of three subjects. In both simulations, source-space ICA achieved higher performance in terms of spatial resolution and ability to separate the two cluster sources. Conversely, both techniques had similar performance on temporal reconstruction of the cluster time-courses. On the reconstruction of real MEG from two subjects with visual stimuli, source-space ICA and sensor-space ICA had near identical performances in terms of temporal reconstruction. The topography of the components between two subjects also showed similar maps. However, source mapping via source-space ICA and sensor-space ICA was dramatically different. The sources found via source-space ICA were mostly concentrated on the cortical areas of the posterior, temporal, and frontal areas. Some of these maps were showing multiple cluster sources associated with one component. On the other hand, sensor-space ICA was only able to provide blurry maps for the components, and some of these maps gave central regions of the brain as the origin of the time-course. Face processing MEG and EEG have a well-established brain activation pattern. Through the literature [35–45] the fusiform gyrus and the temporal gyrus have been shown to be the sources of the N170 and M170 of face processing. A recent paper by Owen *et al* 2012 [46] on the same MEG data used here, shows similar sources found via our approach. They found three regions to be the sources of ERFs of faces: (1) right side of occipital cortex (next to sagittal line) with time-course maximum activity at latencies of 90 ms and 120 ms, (2) one scattered source in occipital cortex with the maximum activity occurring over 180–290 ms, and (3) a bilateral source in the fusiform gyrus (stronger on the right side) with maximum activity at 150–210 ms post stimuli. In addition to these, we found the temporal gyrus and prefrontal cortex, to be substantial

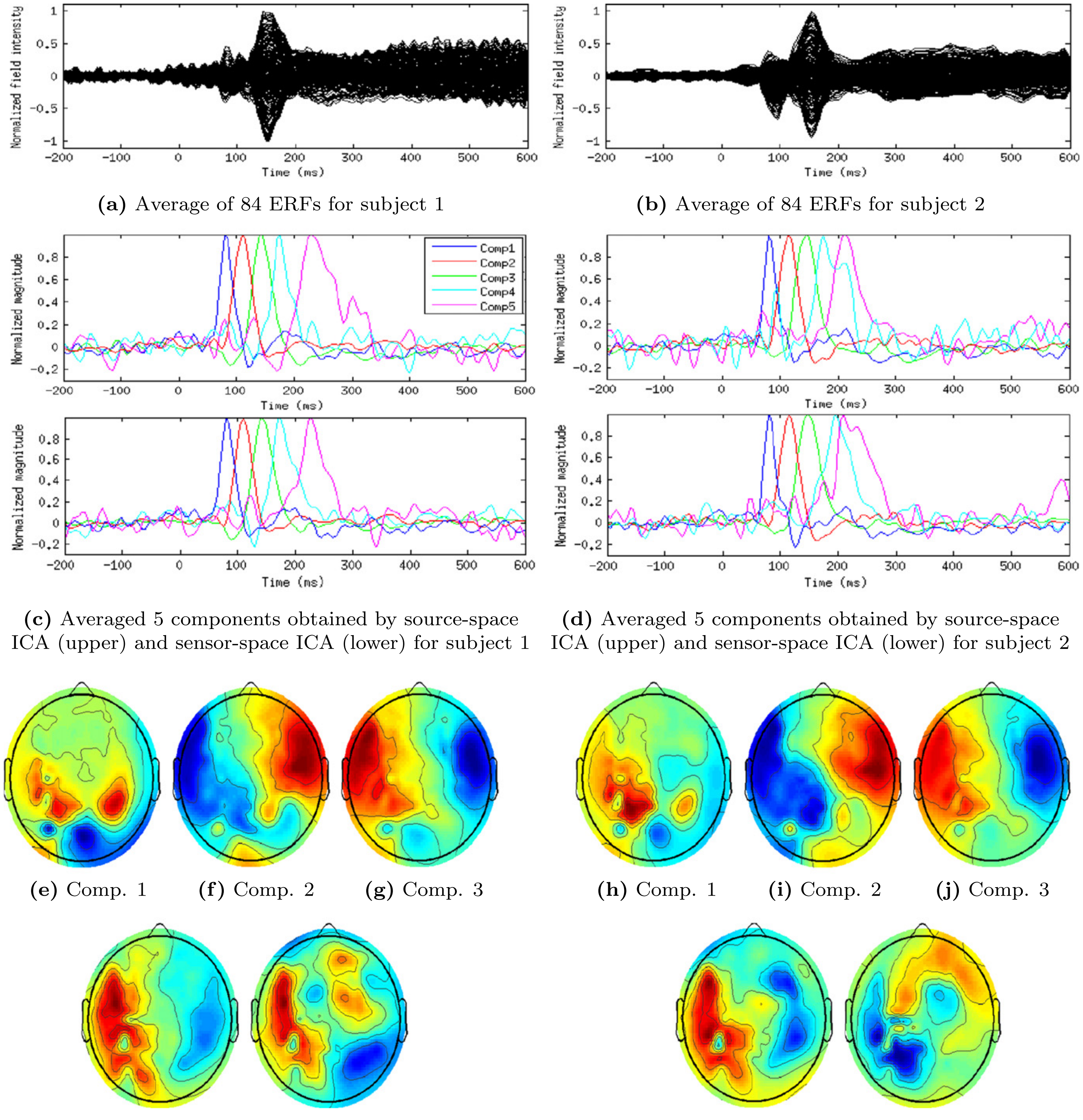

(a) Average of 84 ERFs for subject 1 **(b)** Average of 84 ERFs for subject 2

(c) Averaged 5 components obtained by source-space ICA (upper) and sensor-space ICA (lower) for subject 1 **(d)** Averaged 5 components obtained by source-space ICA (upper) and sensor-space ICA (lower) for subject 2

(e) Comp. 1 **(f)** Comp. 2 **(g)** Comp. 3 **(h)** Comp. 1 **(i)** Comp. 2 **(j)** Comp. 3

(k) Comp. 4 **(l)** Comp. 5 **(m)** Comp. 4 **(n)** Comp. 5

Figure 6. Left column figures belong to subject 1 and the right column to subject 2. Average of 84 ERFs (faces) on 128 channels is shown in figures (a) and (b). The independent time-courses, time-locked to the ERFs, obtained via source-space ICA and sensor-space ICA are shown in figures (c) and (d). The topographic maps of the five independent components for each subjects obtained via sensor-space ICA are shown in figures (e)–(n). The time-courses of the independent components obtained via sensor-space ICA and source-space ICA for each subject are near identical, indicating the similar performance of the two techniques in time-course reconstruction. The topographic maps of the components between two subjects for each independent component are also similar except for component 5.

contributors to face processing. An extensive recent study of face processing MEG [47], which includes data from 17 healthy control subjects as well as 14 patients, shows the right inferior frontal gyrus to be activated at 250 ms post stimuli, which is similar to component 5 shown in figure 7. Another recent study [48] on 24 healthy subjects showed that the right fusiform gyrus and the right inferior occipital gyrus are the sources of M170 for faces. Such sources can be seen on component 3 in figure 7. The results of simulation and real MEG analyses in this paper indicate that sensor-space ICA (e.g., ICA + beamformer/sLORETA/dipole fitting) is not optimal for source localization of multiple cluster sources,

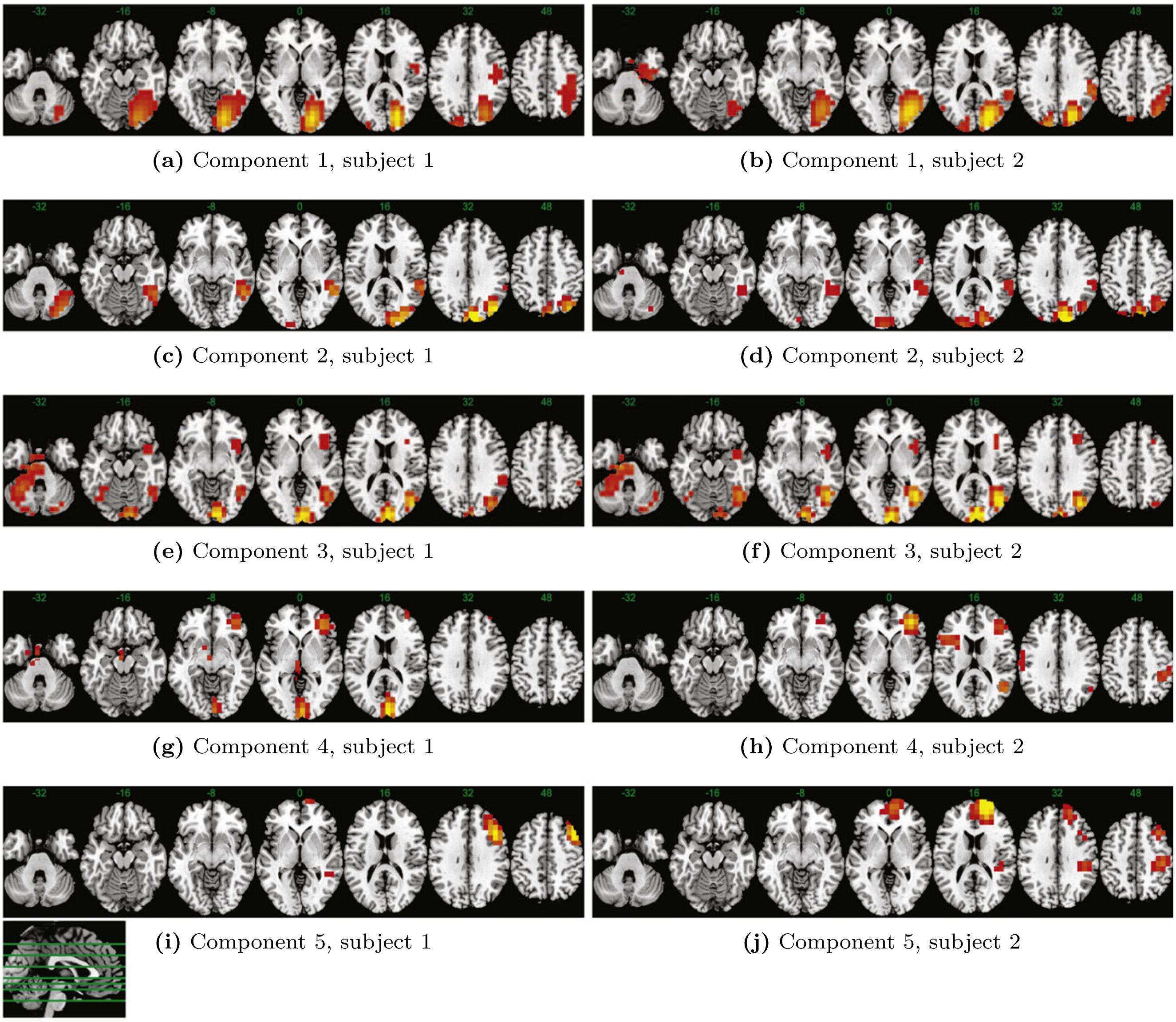

(a) Component 1, subject 1
(b) Component 1, subject 2
(c) Component 2, subject 1
(d) Component 2, subject 2
(e) Component 3, subject 1
(f) Component 3, subject 2
(g) Component 4, subject 1
(h) Component 4, subject 2
(i) Component 5, subject 1
(j) Component 5, subject 2

Figure 7. Figures (a)–(j) are tomographic maps of the five components from the two subjects shown in figure 6. Left-column figures belong to subject 1 and the right-column to subject 2. The maps of the first three components between two subjects are very similar, but components 4 and 5 of the two subjects have differences in patterns of activations. Maps are thresholded at 70% of the voxel with maximum intensity.

even though it is widely applied in the EEG and MEG literature. However, as mentioned earlier, sensor-space ICA performs equally with source-space ICA for simulated single point sources. Also, source-space ICA cannot replace sensor-space ICA in estimating the topographic maps as the mixing matrix of sensor-space ICA is optimal way for topographic maps of components. Traditionally, ICA has been used for extraction of ERPs and as an artefact removal tool on the sensor-space signals. Care should be taken in application of ICA and PCA for artefact removal before inverse modelling. Some of the common artifacts removed by sensor-space ICA are eye movements and eye-blinks. However, such artifacts cover a wide area on the scalp and are highly overlapping with some of the well-known brain sources such as frontal theta rhythm. Removing such artifacts from sensor-signals via ICA can also result in loss of some desired sources. Similarly, removal of sensor-space components manipulates the spatial signature of the remaining signals. Therefore, applying an inverse model on the remaining signals can result in incorrect localization of certain sources, dependent on how much power is lost from such sources due to sensor-space component removal. A trick to avoid losing desired source activity due to sensor-space component removal is to band-pass filter the original data and apply ICA artifact removal on the target frequency bands and sum the artifact-removed band-passed data. This works when the desired sources and artifacts are at different frequencies. Conversely, although we have not demonstrated directly, it is also possible to perform artifact removal via source-space ICA. In this procedure, the inverse technique is applied first and results in attenuation of the artifacts which cannot be interpreted as brain sources in the source-space data. However, due to leakage, some of the powerful noises are still present in the source-space data, as has been shown for eye artifacts [24], and power mapping following inverse modelling will show such artifacts as brain sources. But, by using ICA (and SVD) in the source-space,

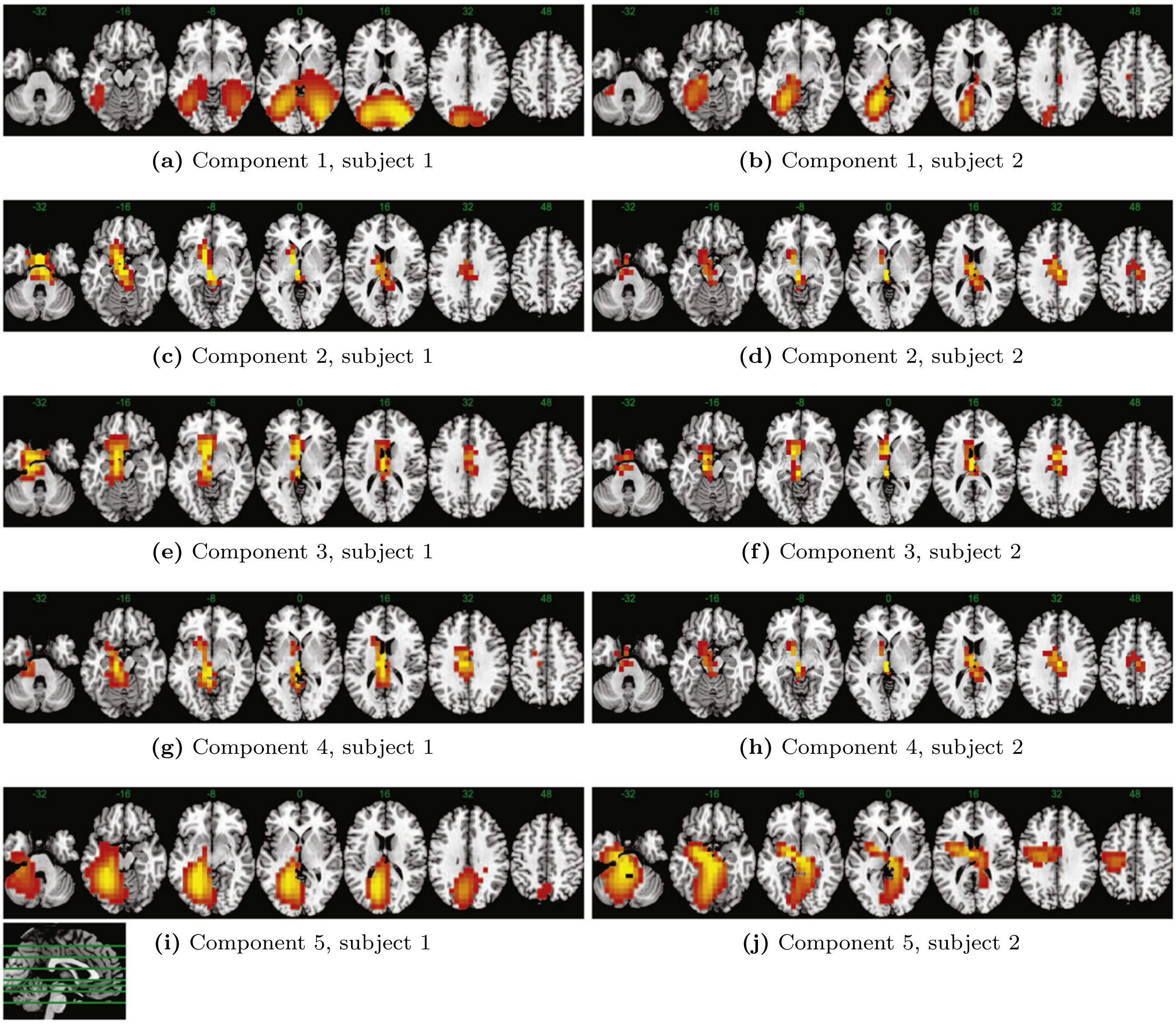

(a) Component 1, subject 1
(b) Component 1, subject 2
(c) Component 2, subject 1
(d) Component 2, subject 2
(e) Component 3, subject 1
(f) Component 3, subject 2
(g) Component 4, subject 1
(h) Component 4, subject 2
(i) Component 5, subject 1
(j) Component 5, subject 2

Figure 8. Figures (a)–(j) are tomographic maps of the five components shown in figure 6. Left-column figures belong to subject 1 and the right-column to subject 2. These maps are obtained via post sensor-space ICA beamforming. The maps of components 2, 3, and 4 between two subjects are similar, but the components 1 and 5 of the two subjects have differences in terms of pattern of the activations. Maps are thresholded at 70% of the voxel with maximum intensity.

such artifacts can be separated from the desired sources and each component has an independent 3D map. We did this when applying source-space ICA to ERFs from facial visual stimuli when we accepted only components time-locked to the stimuli, with remaining components considered to be artifacts and background activity. Other versatile applications of ICA are in connectivity analysis [49, 50] and joint-ICA for extracting common information from two (or more) different functional brain recordings [51–54]. Here, we utilized ICA in source-space and compared in with well established sensor-space ICA for source-localization of MEG sources. While we have determined how the order the application of two conventional techniques (beamforming + ICA versus ICA + beamforming) can change the outcome in source-localization, such comparisons could be extended to more recent signal separation techniques, such as common spatial pattern analysis [55–58] and tensor decomposition [59], which have proven to be practical in brain–computer interfaces [60].

References

[1] Uutela K, Hämäläinen M S and Salmelin R 1983 Global optimization in the localization of neuromagnetic sources *IEEE Trans. Biomed. Eng.* **45** 716–23

[2] Sarvas J 1987 Basic mathematical and electromagnetic concepts of the biomagnetic inverse problem *Phys. Med. Biol.* **32** 11–22

[3] Mosher J C, Lewis P S and Leahy R M 1992 Multiple dipole modeling and localization from spatio-temporal MEG data *IEEE Trans. Biomed. Eng.* **39** 541–57

[4] Hämäläinen M S and Ilmoniemi R J 1994 Interpreting magnetic fields of the brain: minimum norm estimates *Med. Biol. Eng. Comput.* **32** 35–42

[5] Dale A M, Liu A K, Fischl B R, Buckner R L, Belliveau J W, Lewine J D and Halgren E 2000 Dynamic statistical parametric mapping: combining fMRI and MEG for high-resolution imaging of cortical activity *Neuron* **26** 55–67
[6] Pascual-Marqui R D 2002 Standardized low-resolution brain electromagnetic tomography (sLORETA): technical details *Methods Find. Exp. Clin. Pharmacol.* **24** (Suppl. D) 5–12
[7] Van Veen B D, van Drongelen W, Yuchtman M and Suzuki A 1997 Localization of brain electrical activity via linearly constrained minimum variance spatial filtering *IEEE Trans. Biomed. Eng.* **44** 867–80
[8] Robinson S E and Vrba J 1998 Functional neuroimaging by synthetic aperture magnetometry (SAM) *Proc. 11th Int. Conf. on Biomagnetism* ed T Yoshimoto *et al* (Sendai: Tohoku University Press) pp 302–305
[9] Sekihara K, Nagarajan S S, Poeppel D, Marantz A and Miyashita Y 2001 Reconstructing spatio-temporal activities of neural sources using an MEG vector beamformer technique *IEEE Trans. Biomed. Eng.* **48** 760–71
[10] Huang M X *et al* 2004 Commonalities and differences among vectorized beamformers in electromagnetic source imaging *Brain Topogr.* **16** 139–58
[11] Greenblatt R E, Ossadtchi A and Pflieger M E 2005 Local linear estimators for the linear bioelectromagnetic inverse problem *IEEE Trans. Biomed. Eng.* **53** 3403–12
[12] Sekihara K and Nagarajan S S 2008 *Adaptive Spatial Filters for Electromagnetic Brain Imaging* (Berlin: Springer)
[13] Brookes M J, Hale R J, Zumer J M, Stevenson C M, Francis S T, Barnes G R, Owen P J, Morris P G and Nagarajan S S 2011 Measuring functional connectivity using MEG: methodology and comparison with fcMRI *NeuroImage* **56** 1082–104
[14] Jonmohamadi Y, Krueger R, Weiss D, Poudel G, Innes C and Jones R 2014 Comparison of beamformers for EEG source signal reconstruction *Biomed. Signal Process. Control* **14** 175–88
[15] Sanei S and Chambers J A 2007 *EEG Signal Processing* (Chichester: Wiley)
[16] Onton J, Westerfield M, Townsend J and Makeig S 2006 Imaging human EEG dynamics using independent component analysis *Neurosci. Biobehav.* Rev. **30** 808–22
[17] Makeig S, Debener S, Onton J and Delorme A 2004 Mining event-related brain dynamics *Trends Cogn. Sci.* **8** 204–10
[18] Jervis B *et al* 2007 The independent components of auditory P300 and CNV evoked potentials derived from single-trial recordings *Physiol. Meas.* **28** 745–71
[19] Ventouras E M, Ktonas P Y, Tsekou H, Paparrigopoulos T, Kalatzis I and Soldatos C R 2010 Independent component analysis for source localization of EEG sleep spindle components *Comput. Intell. Neurosci.* **2010** 1–2
[20] La Foresta F, Mammone N and Morabito F C 2009 PCAICA for automatic identification of critical events in continuous coma-EEG monitoring *Biomed. Signal Process. Control* **4** 229–35
[21] Jonmohamadi Y, Poudel G, Innes C and Jones R 2014 Voxel-ICA for reconstruction of source signal time-series and orientation in EEG and MEG *Australas. Phys. Eng. Sci. Med.* **37** 457–64
[22] Jung T P, Humphries C, Lee T W, Makeig S, McKeown M J, Iragui V and Sejnowski T J 1998 Extended ICA removes artifacts from electroencephalographic recordings *Adv. Neural Inf. Process. Syst.* **10** 894–900
[23] Jung T P, Makeig S, Humphries C, Lee T W, McKeown M J, Iragui V and Sejnowski T J 2000 Removing electroencephalographic artifacts by blind source separation *Psychophysiology* **37** 163–78
[24] Fatima Z, Quraan M A, Kovacevic A R and McIntosh N 2013 ICA-based artifact correction improves spatial localization of adaptive spatial filters in MEG *NeuroImage* **78** 284–94
[25] Jonmohamadi Y, Poudel G, Innes C and Jones R 2014 Source-space ICA for EEG source separation, localization, and time-course reconstruction *NeuroImage* **101** 720–37
[26] Pascual-Marqui R D 2007 Discrete, 3D distributed, linear imaging methods of electric neuronal activity. Part 1: Exact, zero error localization (arXiv:0710.3341)
[27] Gross J and Ioannides A A 1999 Linear transformations of data space in MEG *Phys. Med. Biol.* **44** 2081–97
[28] Cox H, Zeskind R and Owen M 1987 Robust adaptive beamforming *IEEE Trans. Acoust. Speech Signal Process. (ASSP)* **35** 1365–76
[29] Baker A P, Brookes M J, Rezek I A, Smith S M, Behrens T, Smith P J P and Woolrich M 2014 Fast transient networks in spontaneous human brain activity *eLife* **3** 01867
[30] Oostenveld R, Fries P, Maris E and Schoffelen J M 2011 Fieldtrip: open source software for advanced analysis of MEG, EEG, and invasive electrophysiological data *Comput. Intell. Neurosci.* **2011** 1–9
[31] Bell A J and Sejnowski T J 1995 An information-maximization approach to blind separation and blind deconvolution *Neural Comput.* **7** 1129–59
[32] Cheyne D, Bakhtazad L and Gaetz W 2006 Spatiotemporal mapping of cortical activity accompanying voluntary movements using an event-related beamforming approach *Hum. Brain Mapp.* **27** 213–29
[33] Quraan M A and Cheyne D 2010 Reconstruction of correlated brain activity with adaptive spatial filters in MEG *NeuroImage* **49** 2387–400
[34] Robinson S E 2004 Localization of event-related activity by SAM(erf) *Neurol. Clin. Neurophysiol.* **2004** 109
[35] Botzel K, Schulze S and Stodieck S R 1995 Scalp topography and analysis of intracranial sources of face-evoked potentials *Exp. Brain Res.* **104** 135–43
[36] Deffke I, Sander T, Heidenreich J, Sommer W, Curio G, Trahms L and Lueschow A 2007 MEG/EEG sources of the 170 ms response to faces are co-localized in the fusiform gyrus *NeuroImage* **35** 1495–501
[37] Halgren E, Raij T, Marinkovic K, Jousmaki V and Hari R 2000 Cognitive response profile of the human fusiform face area as determined by MEG *Cereb. Cortex* **10** 69–81
[38] Pizzagalli D A, Lehmann D, Hendrick A M, Regard M, Pascual-Marqui R D and Davidson R J 2002 Affective judgments of faces modulate early activity (approximately 160 ms) within the fusiform gyri *NeuroImage* **16** 663–77
[39] Schweinberger S R, Pickering E C, Jentzsch I, Burton A M and Kaufmann J M 2002 Event-related brain potential evidence for a response of inferior temporal cortex to familiar face repetitions *Cogn. Brain Res.* **14** 398–409
[40] Shibata T, Nishijo H, Tamura R, Miyamoto K, Eifuku S, Endo S and Ono T 2002 Generators of visual evoked potentials for faces and eyes in the human brain as determined by dipole localization *Brain Topogr.* **15** 51–63
[41] Swithenby S J, Bailey A J, Brautigam S, Josephs O E, Jousmaki V and Tesche C D 1998 Neural processing of human faces: a magnetoencephalographic study *Exp. Brain Res.* **118** 501–10
[42] Tanskanen T, Nasanen R, Montez T, Paallysaho J and Hari R 2005 Face recognition and cortical responses show similar sensitivity to noise spatial frequency *Cereb. Cortex* **15** 526–34
[43] Tarkiainen A, Cornelissen P L and Salmelin R 2002 Dynamics of visual feature analysis and object-level processing in face versus letter-string perception *Brain* **125** 1125–36
[44] Watanabe S, Kakigi R, Koyama S and Kirino E 1999 Human face perception traced by magneto- and electro-encephalography *Cogn. Brain Res.* **16** 125–42
[45] Karnath H O 2001 New insights into the functions of the superior temporal cortex *Nat. Rev. Neurosci.* **2** 568–76

[46] Owen J P, Wipf D P, Attias H T, Sekihara K and Nagarajan S S 2012 Performance evaluation of the champagne source reconstruction algorithm on simulated and real M/EEG data *Neuroscience* **60** 305–23
[47] Rivolta D *et al* 2014 Source-reconstruction of event-related fields reveals hyperfunction and hypofunction of cortical circuits in antipsychotic-naive, first-episode schizophrenia patients during mooney face processing *J. Neurosci.* **34** 5909–17
[48] Gao Z, Goldstein A, Harpaz Y, Hansel M, Zion-Golumbic E and Bentin S 2013 A magnetoencephalographic study of face processing: M170, gamma-band oscillations and source localization *Hum. Brain Mapp.* **34** 1783–95
[49] Luckhoo H, Hale J R, Stokes M G, Nobre A C, Morris P G, Brookes M J and Woolrich M V 2012 Inferring task-related networks using independent component analysis in magnetoencephalography *NeuroImage* **62** 530–41
[50] Aoki Y, Ishii R, Pascual-Marqui R D, Canuet L, Ikeda S, Hata K M H M T, Imajo M, Asada T, Iwase M and Takeda M 2015 Detection of EEG-resting state independent networks by eLORETA-ICA method *Front. Hum. Neurosci.* **9** 1–2
[51] Calhoun V D, Adali T, Kiehl K A, Astur R, Pekar J J and Pearlson G D 2006 A method for multitask fMRI data fusion applied to schizophrenia *Hum. Brain Mapp.* **27** 598–610
[52] Sui J, Adali T, Pearlson G, Yang H, Sponheim S, White T and Calhoun V 2010 A CCA+ICA based model for multi-task brain imaging data fusion and its application to schizophrenia *NeuroImage* **51** 123–34
[53] Sui J, Pearlson G, Caprihan A, Adali T, Kiehl K A, Liu J, Yamamoto J and Calhoun V D 2011 Discriminating schizophrenia and bipolar disorder by fusing fMRI and DTI in a multimodal CCA+ joint ICA model *NeuroImage* **57** 839–55
[54] Stephen J M, Coffman B A, Jung R E, Bustillo J R, Aine C J and Calhoun V D 2013 Using joint ICA to link function and structure using MEG and DTI in schizophrenia *NeuroImage* **83** 418–30
[55] Blankertz B, Tomioka R, Lemm S, Kawanabe M and Muller K 2008 Optimizing spatial filters for robust EEG single-trial analysis *IEEE Signal Process. Mag.* **25** 41–56
[56] Lotte F and Guan C 2011 Regularizing common spatial patterns to improve BCI designs: unified theory and new algorithms *IEEE Trans. Biomed. Eng.* **58** 355–62
[57] Nikulin V V, Nolte G and Curio G 2011 A novel method for reliable and fast extraction of neuronal EEG/MEG oscillations on the basis of spatio-spectral decomposition *NeuroImage* **55** 1528–35
[58] Sannelli C, Vidaurre C, Müller K R and Blankertz B 2011 Common spatial pattern patches—an optimized filter ensemble for adaptive BCIs *J. Neural Eng.* **8** 025012
[59] Cong F, Lin Q H, Kuang L D, Gong X F, Astikainen P and Ristaniemi T 2015 Tensor decomposition of EEG signals: a brief review *J. Neurosci. Methods* **248** 59–69
[60] Tangermann M *et al* 2012 Review of the BCI competition IV *Front. Neurosci.* **13** 6–55